Inorganic Chemistry

Article

pubs.acs.org/IC

Low-Temperature Diffusion of Oxygen through Ordered Carbon Vacancies in Zr_2C_x: The Formation of Ordered $Zr_2C_xO_y$

Wentao Hu, Jianyong Xiang, Shaocun Liu, Yang Zhang, Cankun Chen, Pang Wang, Haitao Wang, Fusheng Wen, Bo Xu, Julong He, Dongli Yu, Yongjun Tian,* and Zhongyuan Liu*

State Key Laboratory of Metastable Materials Science and Technology, Yanshan University, Qinhuangdao 066004, China

Supporting Information

ABSTRACT: Investigations are performed on low-temperature oxygen diffusion in the carbon vacancy ordered $ZrC_{0.6}$ and thus induced formation of the oxygen atom ordered $ZrC_{0.6}O_{0.4}$. Theoretically, a superstructure of Zr_2CO can be constructed via the complete substitution of carbon vacancies with O atoms in the Zr_2C model. In the ordered $ZrC_{0.6}$, the consecutive arrangement of vacancies forms the vacancy channels along some zone axes in the C sublattice. Through these vacancy channels, the thermally activated oxygen diffusion is significantly facilitated. The oxygen atoms diffuse directly into and occupy the vacancies, producing the ordered $ZrC_{0.6}O_{0.4}$. Relative to the ordered $ZrC_{0.6}$, the Zr positions are finely tuned in the ordered $ZrC_{0.6}O_{0.4}$ because of the ionic Zr−O bonds. Because of this fine adjustment of Zr positions and the presence of oxygen atoms, the superstructural reflections are always observable in a selected area electron diffraction (SAED) pattern, despite the invisibility of superstructural reflections in $ZrC_{0.6}$ along some special zone axes. Similar to the vacancies in ordered $ZrC_{0.6}$, the ordering arrangement of O atoms in the ordered $ZrC_{0.6}O_{0.4}$ is in nanoscale length, thus forming the nano superstructural domains with irregular shapes.

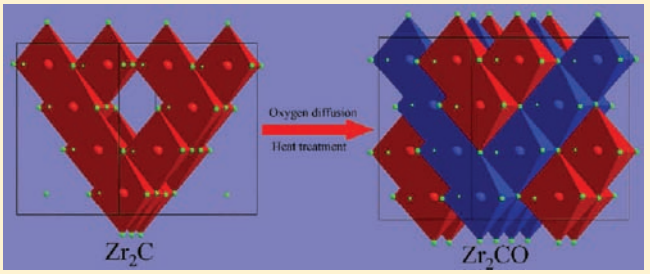

1. INTRODUCTION

Zirconium carbide (ZrC) is one of the important refractory materials, exhibiting many excellent properties such as high hardness, good corrosion resistance, good electrical and thermal conductivity, and so forth.[1−3] Because of these attractive properties, ZrC demonstrates great potential in technological applications, especially those under extreme conditions of temperature and pressure. Moreover, owing to the low neutron absorption or scattering cross sections, low damage under irradiation,[4] ZrC is considered as the primary option for a component of TRISO fuel particles in future nuclear reactors.[5] Unfortunately, these attractive potential applications are restricted by the poor oxidation resistance of ZrC. In the previous studies on the oxidation of ZrC,[6−8] it is reported that the oxygen diffusion occurs mainly through the grain boundaries, and via the substitution of C atoms by O atoms, an intermediate ultrathin layer of oxycarbide is formed in the first stage of oxidation to ZrO_2.

It is well-known that zirconium carbide of ZrC_x is highly nonstoichiometric. Thanks to the high sensitivity of the chemical bonding and electronic structures to the carbon vacancies, the nonstoichiometric carbides usually exhibit significantly different properties from the stoichiometric ones.[9] For the nonstoichiometric carbides, the ordering arrangement of carbon vacancies has been believed to favor the enhancement of hardness[10−14] and yield stress.[15,16] Similarly, their potential applications are subject to the influence of chemical stability at high temperature. To date, however, there has been no report on oxidation of the nonstoichiometric carbides with the ordered carbon vacancies, especially the role of ordered vacancies in oxidation. This is probably due to the difficulty for the sintering of ordered nonstoichiometric carbides. Using the conventional routes such as hot pressing (HP) and hot isostatic pressing (HIP), the sintered nonstoichiometric carbides are generally disordered, although the synthesis of ordered TiC_x has been reported via the reactive HP route.[17] To achieve the ordering arrangement of carbon vacancies, complicated post annealing is required, and it can be as long as several hundred hours.[18−20] In our recent investigations on the syntheses of titanium carbides,[21] it has been found that the nonstoichiometric TiC_x with ordered carbon vacancies can be directly prepared by spark plasma sintering (SPS) of the mechanochemically synthesized TiC_x nanopowders. Using the same synthesis route, the nonstoichiometric $ZrC_{0.6}$ with ordered carbon vacancies has also been obtained.

The present work is focused to the enhanced oxygen diffusion via the ordered carbon vacancies in the SPS-sintered $ZrC_{0.6}$ at low temperature and thus induced formation of the ordered phase of oxycarbide $ZrC_{0.6}O_{0.4}$. It is found that the presence of ordered carbon vacancies favors the oxygen atoms to diffuse into and occupy the vacancies. Similar to the ordered carbon vacancies, the ordering occupancy of oxygen atoms leads to the formation of an ordered phase of $ZrC_{0.6}O_{0.4}$.

Received: January 3, 2012
Published: April 9, 2012

   dx.doi.org/10.1021/ic300014a | Inorg. Chem. 2012, 51, 5164−5172

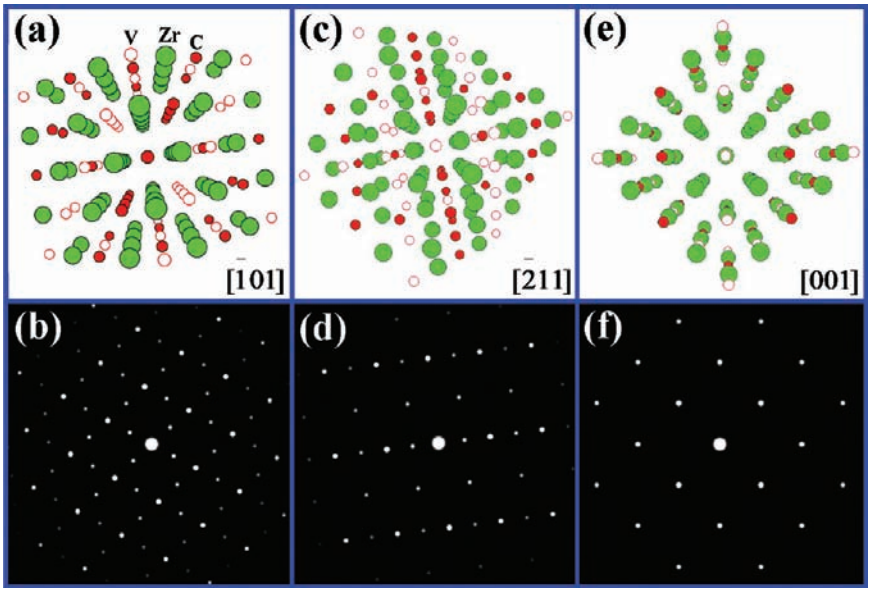

Figure 1. (**a, c, e**) The constructed structures from the superstructural model of Zr_2C proposed by Gusev and Rempel, which are viewed along the zone axes of $[\bar{1}01]$, $[\bar{2}11]$, and [001], respectively. (**b, d, f**) The corresponding simulated SAED patterns along these three zone axes. In the SAED patterns along the $[\bar{1}01]$, $[\bar{2}11]$ zone axes, in addition to the reflections from the parent rocksalt structure, a set of weak reflections are observable from the superstructure of ordered vacancies. Along the [001] axis, however, the superstructural reflections are invisible.

2. EXPERIMENTAL SECTION

2.1. Sample Synthesis. The starting nanopowders of ZrC_x were synthesized by high-energy ball milling of Zr powders (−325 mesh, purity 99.5%) in toluene (HPLC grade, 99.7%, Alpha Aesar, U.S.A.) in a planetary ball miller (Fritsch P4, Germany). The detailed information was introduced in our previous work.[22] In the present work, some milling and sintering parameters have been optimized. The ratio of toluene and Zr powders was changed to be 2.5:1, and the rotation speed during milling was set to be 500 rpm. The nonstoichiometric $ZrC_{0.6}$ with ordered carbon vacancies was prepared by spark plasma sintering of the nanopowders of ZrC_x obtained after the 6-h milling. The preparation was performed in a DR. SINTER type SPS 3.20MK-IV (Sumitomo Coal Mining, Japan) along the same route as that previously reported for nonstoichiometric TiC_x.[21] The as-milled nanopowders of ZrC_x were loaded in a graphite die (20 mm in diameter) for sintering. The sintering process started by the first application of a 50 MPa compressive pressure and then the rapid heating of 50 °C/min to 700 °C. After soaking at 700 °C for 30 min, the heating of 50 °C/min was continued to 1600 °C. After keeping the temperature at 1600 °C for 5 min, the applied current was reduced and the pressure was released with the specimen cooling down in the chamber. The sample with 10 mm in thickness and 20 mm in diameter was finally obtained, and then polished to remove any surface carbon contamination. The C/Zr ratio in the sintered sample was first determined to be 0.61 via the complete oxidation to ZrO_2 in air at 1000 °C in a homemade tubular furnace. However, the measurement of Raman spectroscopy indicates the detectable residual carbon in the sintered sample. Thus, the x of ZrC_x should be overestimated. The value of x was finally refined to be 0.58 from the mass increase owing to oxygen diffusion during the isothermal heat treatments.

2.2. Nonisothermal and Isothermal Heat Treatments. The nonisothermal heating of the ordered $ZrC_{0.6}$ was performed in a furnace with a flow of a mixture of Ar/O_2 gas at atmospheric pressure (the oxygen partial pressure was adjusted to ~0.5 Pa). During the heating up from room temperature (RT) to 430 °C at a rate of 2 °C per min, in situ X-ray diffraction (XRD) patterns were collected at different temperatures. The isothermal heating was carried out in a homemade tubular furnace at a series of temperatures under atmospheric conditions. The sample was first heated up to the required temperature in a flow of Ar gas (99.99% purity) and held for 10 min. Afterwards, the flow of Ar gas was terminated, and the sample was heated under atmospheric conditions at the required temperature for 600 min. Finally, the sample was taken out of the furnace to cool down. During the isothermal heating, the mass change was monitored.

2.3. Characterization. In situ high-temperature X-ray diffraction (HTXRD) and room-temperature (RT) XRD were performed using a diffractometer of D/Max-2500PC with Cu K_α radiation (λ = 1.5406 Å) at 200 mA and 40 kV. The scan speed was set to be 2°/min. The Rietveld refinements of the XRD patterns were performed using the software of MAUD. The morphology of the fracture surfaces of the sample was checked using a field emission scanning electron microscope (FE-SEM) (S4800, HITACHI, Japan) with accelerating voltage of 20 kV. A JEM-2010 transmission electron microscope (TEM) (JEOL, Japan) at 200 kV was used to do the measurements of the TEM image, selected area electron diffraction (SAED), and high resolution TEM (HRTEM) image. The X-ray energy dispersive spectra (XEDS) were taken using the INCA (Oxford, England).

3. RESULTS AND DISCUSSION

3.1. Nano Superstructural Domains in Ordered $ZrC_{0.6}$. In the nonstoichiometric ZrC_x with the proper carbon contents, the carbon vacancies can be aligned in an ordering way in the C sublattice, forming a superstructure. Gusev and Rempel[9] proposed a superstructural model of Zr_2C with the space group of $Fd\bar{3}m$, in which the C and Zr atoms are located at positions of 16d (5/8 5/8 5/8) and 32e (3/8 3/8 3/8), respectively, while the carbon vacancies are considered to be at position of 16c (1/8 1/8 1/8). Figures 1a, 1c and 1e show the crystal models viewed along the $[\bar{1}01]$, $[\bar{2}11]$, and [001] zone axes, respectively. Owing to the ordered carbon vacancies, the $(111)_C$ planes of the C sublattice can be divided into two types A and B (also see Supporting Information, Figure S1). In type A, 2/3 positions are occupied by C atoms and the rest are the vacancies, and only 1/3 positions are occupied by C atoms with the rest being the vacancies in type B. Along the $[\bar{1}01]$ zone axis, the vacancy channels (V-channels) and the carbon strings (C-strings) are constructed by the consecutive arrangement of the carbon vacancies and C atoms, respectively, while the alternative alignment of carbon vacancies and C atoms forms the carbon−vacancy strings (C + V strings). The type-A (B)

dx.doi.org/10.1021/ic300014a | Inorg. Chem. 2012, 51, 5164−5172

$(111)_C$ planes are composed of the alternative arrangement of the C+V strings and the V-channels (C strings). The C sublattice of Zr_2C is formed by the alternative stacking of A and B types of $(111)_C$ planes along the [111] direction. This particularly ordered carbon vacancies form a cubic superstructure in the C sublattice. On the basis of this superstructural model of Zr_2C, the calculated XRD pattern predicts that, in addition to the standard diffraction peaks owing to the parent rocksalt structure, a set of extra weak peaks should appear because of the superstructure of ordered carbon vacancies.[9] In the theoretically simulated SAED patterns (Figure 1b, 1d and 1f), in addition to the reflections from the parent rocksalt structure, the ordered carbon vacancies induce the appearance of the superstructural reflections along some zone axes. However, the superstructural reflections are invisible along some special zone axes because of the particular ordering arrangement of carbon vacancies, for example, along the [001] zone axis.

The crystal structure of the ordered $ZrC_{0.6}$ was characterized by the measurements of XRD and SAED. The SEM image for fracture surface of $ZrC_{0.6}$ (inset of Figure 2) displays an average

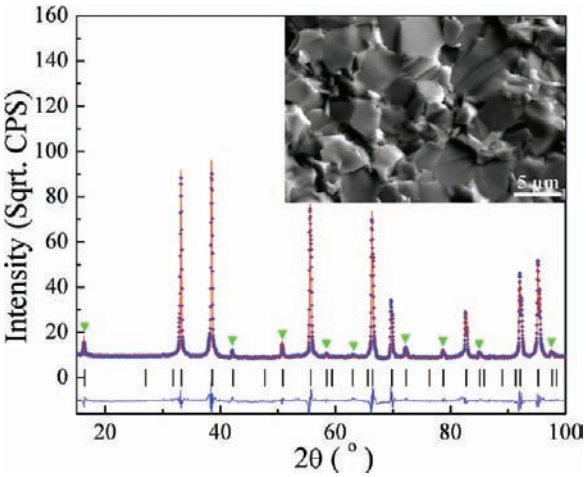

Figure 2. Experimental XRD spectrum (blue diamonds) and the Rietveld refinement result (solid line) for the ordered $ZrC_{0.6}$. The solid curve on the bottom shows the difference between the experimental and calculated results. The vertical bars in the middle represent the positions of all possible reflections peaks. The inset is the TEM image for the fracture surface of ordered $ZrC_{0.6}$. The superstructural peaks are marked with green upside down triangles.

grain size of ~5 um. The XRD measurement shows a set of interesting weak Bragg peaks as well as the standard peaks of the rocksalt structured $ZrC_{0.6}$ (Figure 2). These weak peaks are recognized to be consistent in positions with the calculated ones for the cubic superstructure of Zr_2C.[9] On the basis of the superstructural model of Zr_2C with space group of $Fd\bar{3}m$, Rietveld refinement of the XRD pattern is performed. As shown in Figure 2, the calculated XRD pattern is in good agreement with the experimental XRD one (refer to Table 1 for the refinement parameters). The unit cell parameter of superstructural phase of Zr_2C is determined to be 0.93236 nm. Figure 3 shows the TEM images of a broken piece of the ordered $ZrC_{0.6}$ and the SAED patterns taken along three zone axes of $[\bar{1}01]$, $[\bar{2}11]$, and [001]. These experimental SAED patterns are consistent with the theoretically simulated ones of Zr_2C. In the SAED patterns along the zone axes of $[\bar{1}01]$ and $[\bar{2}11]$, in addition to the reflections produced by the rocksalt structure of

Table 1. Refined Parameters for Carbon Vacancies Ordered $ZrC_{0.6}$ Obtained from Rietveld Refinement of Powder XRD Pattern

atom	x	y	z	occupation	B_{iso} (Å^2)
C	0.1250	0.1250	0.1250	1	2.68
Zr	0.3716	0.3716	0.3716	1	2.22

*The X-ray wavelength is 0.154056 nm. The unit cell parameter of superstructural phase of Zr_2C is determined to be 0.93236(1) nm. The space group is $Fd\bar{3}m$. R factors, Sig. =1.52, R_w = 12.1%, R_{exp}= 7.225%. The displacement of Zr atoms from the ideal position of 32(e) (0.3750) is 0.0034.

$ZrC_{0.6}$, superstructural reflections are also observed because of the ordered carbon vacancies. Along the [001] zone axis, however, the superstructural reflections are not visible. Thus, the measurements of XRD and SAEDs are combined together to confirm the cubic superstructure of ordered carbon vacancies in the C sublattice of $ZrC_{0.6}$.

The dark-field (DF) images in Figure 3e and 3f are taken from the reflection of (111) and the superstructural reflection of 1/2(111) along the $[\bar{1}01]$ zone axis, respectively. The DF image in Figure 3e shows the relatively uniform contrast, indicating the uniform contribution to the reflection from the parent rocksalt structure. However, the DF image in Figure 3f demonstrates that the contributions to superstructural reflection come from separated nano domains. In other words, the ordered carbon vacancies have the nanoscale length of ordering, thus forming the separate nano superstructural domains with the irregular shape.

3.2. Nonisothermal Heating in an Ar/O_2 Mixture. A polished sheet of the ordered $ZrC_{0.6}$ sample was heated in a furnace from RT to 430 °C at a rate of 2 °C per min. As shown in Figure 4a, in situ XRD patterns were collected at a series of temperatures during the heating up. Only a small amount of t-ZrO_2 is observed to appear when the temperature is elevated to 400 °C and above. Thus, the oxidation to ZrO_2 is negligible in the low temperature range of $T \leq 430$ °C. Before the heat treatment, no sign of oxygen is detectable in the sheet of ordered $ZrC_{0.6}$. After the heating, however, the presence of oxygen is observed by XEDS (see Supporting Information, Figure S2a), being indicative of the diffusion of oxygen atoms into the lattice of ordered $ZrC_{0.6}$. It is interesting to note that the sample changes in color from silver gray to golden yellow owing to the heating (see insets of Supporting Information, Figure S2a). This color change is attributed to the diffusion of oxygen atoms into the lattice. Moreover, even without any heat treatment, the color change to golden yellow also occurs after the long-time exposure under atmospheric environment (see Supporting Information, Figure S2b). This observation implies that the presence of ordered carbon vacancies facilitate the oxygen diffusion into the lattice.

In the nonstoichiometric ZrC_x, the oxygen atoms can occupy the carbon vacancies or replace the carbon atoms to form an oxycarbide phase of ZrC_xO_y.[23−25] The occupation of carbon vacancies or the substitution of C with O does not modify the rocksalt structure.[26−28] The oxycarbide of ZrC_xO_y is thus isostructural to ZrC_x with the similar cell parameters. Similar to ZrC_x, ZrC_xO_y is also able to exist over a wide range of nonstoichiometry, and its lattice parameters depend on the content of oxygen.[25] In the stoichiometric ZrC, the oxygen diffusion occurs mainly through the grain boundaries.[6−8] In the ordered $ZrC_{0.6}$, the ordering arrangement of carbon vacancies in

dx.doi.org/10.1021/ic300014a | Inorg. Chem. 2012, 51, 5164−5172

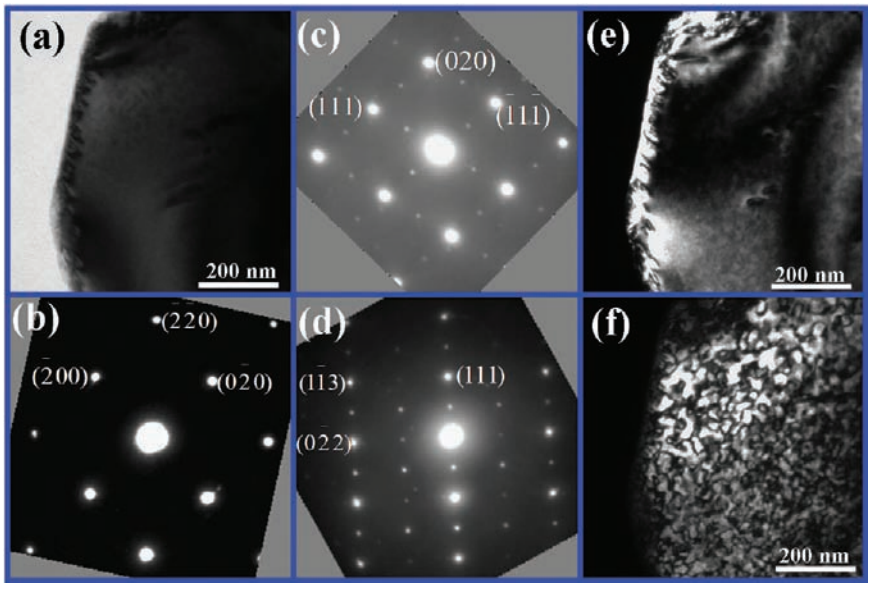

Figure 3. (**a**) BF TEM image of a broken piece of the ordered $ZrC_{0.6}$. The SAED patterns are taken along three different zone axes of [001] (**b**), [$\bar{1}$01] (**c**), and [$\bar{2}$11] (**d**). In the SAED pattern along the [$\bar{1}$01] and [$\bar{2}$11] axes, the reflections from the parent rocksalt structure and the superstructural reflections induced by ordered vacancies are simultaneously observable. In the SAED pattern along the [001] axis, no superstructure reflections are visible. (**e, f**) The DF TEM images obtained by using the (111) reflection and the superstructural 1/2(111) reflection along the [$\bar{1}$01] axis, respectively.

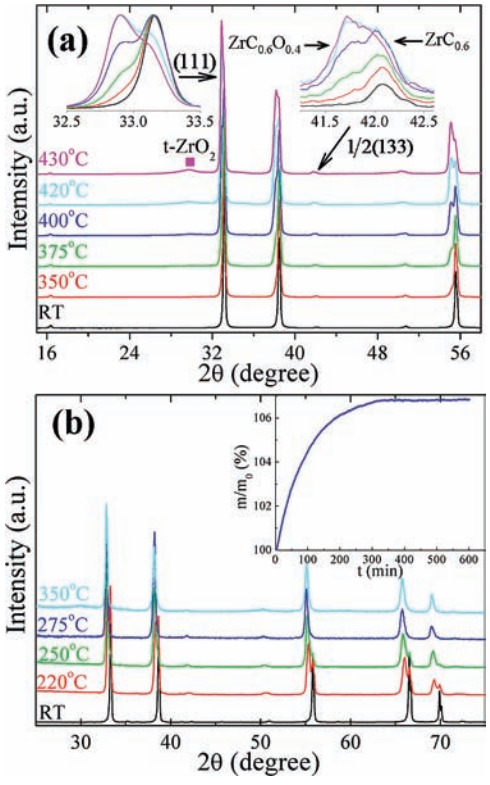

Figure 4. (**a**) In situ XRD patterns collected at different temperatures during the nonisothermal heating from RT to 430 °C. Insets are the exemplified (111) peak (left) and superstructural 1/2(133) peak (right). (**b**) The XRD spectra obtained at RT after the isothermal heating at different temperatures for 600 min. Inset is the change in mass with time during the isothermal heating at 275 °C.

the C-sublattice leads to the presence of vacancy channels (see Supporting Information, Figures S1c and S1d). These vacancy channels provide additional fast tracks for the oxygen diffusion. As observed in Figure 4a, just insignificant oxidation to ZrO_2 occurs during the heating at relatively high temperature. Thermodynamically, the thermal energy at low temperature is not high enough to activate the replacement of C atoms with O atoms. Instead, the O atoms just go directly into and occupy the carbon vacancies through the vacancy channels, forming the phase of oxycarbide $ZrC_{0.6}O_y$ ($y \leq 0.42$).

In the literature, it was reported that the cell parameters of ZrC_xO_y ($y = 1 - x$) are a little smaller than those of the stoichiometric ZrC, or in other words, the Bragg reflection peaks of ZrC_xO_y in the XRD patterns are shifted a little toward the high-angle direction relative to those corresponding peaks of ZrC.[25,29,30] As shown in Figure 4a and insets, however, the reflection peaks of $ZrC_{0.6}O_y$ are shifted a little toward the low-angle direction with respect to the corresponding peaks of the ordered $ZrC_{0.6}$. This is because the unit cell parameter of the superstructural phase Zr_2C (9.3236 Å) is smaller than the doubled unit cell parameter of ZrC (4.693 Å, JCPDS No. 35-0784). With the increase of temperature, the phase of $ZrC_{0.6}O_y$ increases gradually in quantity owing to the persistent diffusion of oxygen to the vacancies. Thus, the reflection peaks of $ZrC_{0.6}O_y$ are observed to continuously increase in intensity. This is shown more obviously in the amplified (111) peak (inset in Figure 4a). At $T \geq 400$ °C, the peaks become comparable in intensity to the corresponding ones of the ordered $ZrC_{0.6}$. Accompanying the appearance of $ZrC_{0.6}O_y$, new weak diffraction peaks appear simultaneously on the low-angle sides of the superstructural peaks of ordered vacancies, and become stronger in intensity with the rise of temperature. As an example, the inset of Figure 4a displays the amplified peak of 1/2(133). On the basis of these observations of the in situ high-temperature XRD patterns, it can be considered that the vacancy channels formed by the ordered carbon vacancies in the C sublattice facilitate the diffusion of oxygen during the heating. The oxygen atoms diffuse easily into the carbide of $ZrC_{0.6}$ through the vacancy channels, occupying the vacancies and forming the oxycarbide of ZrC_xO_y. The appearance of

dx.doi.org/10.1021/ic300014a | Inorg. Chem. 2012, 51, 5164−5172

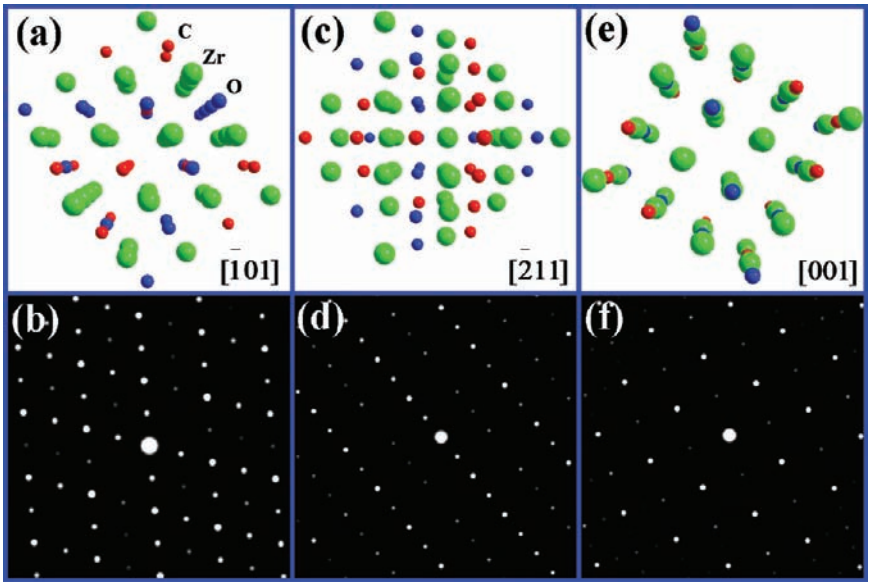

Figure 5. (**a, c, e**) Constructed structures of Zr_2CO on the basis of the superstructural model of Zr_2C, which are viewed along three different zone axes of $[\bar{1}01]$, $[\bar{2}11]$, and [001], respectively. (**b, d, f**) The corresponding simulated SAED patterns along these three zone axes. In contrast to the invisibility of superstructural reflections from the ordered vacancies in Zr_2C along the [001] zone axis, the superstructural reflections owing to ordered O atoms are always observable.

these new weak peaks suggests that the occupancy of oxygen atoms in the vacancies should be ordered in the C-sublattice, similar to the ordered carbon vacancies. This is interesting but unexpected. In the investigated temperature range, the weak superstructural peaks of ordered carbon vacancies remain observable. The ordering arrangement of carbon vacancies are not destroyed by the diffusion of O atoms into vacancies. By taking into consideration the oxygen diffusion from outside to inside, the simultaneous observation of the ordered $ZrC_{0.6}$ and the ordered $ZrC_{0.6}O_y$ suggests that the oxygen atoms are not thermally activated to diffuse into the whole C sublattice. The oxygen atoms just diffuse inside to a certain depth, leading to the formation of an outside layer of the ordered $ZrC_{0.6}O_y$, while the ordered $ZrC_{0.6}$ still exists inside. With the elevation of temperature, the O atoms diffuse deeper into the C sublattice and occupy more vacancies from outside to inside. Thus, this layer of the ordered $ZrC_{0.6}O_y$ becomes thicker. However, the oxygen content of y in $ZrC_{0.6}O_y$ is not dependent on the temperature. This is supported by the in situ XRD patterns at different temperatures. Insets of Figure 4a display that the positions of the (111) peak and 1/2(133) superstructural peak are almost fixed. Most probably, the value of y is equal or at least close to 0.42. For both $ZrC_{0.6}$ and $ZrC_{0.6}O_y$, the quantified unit cell parameters are determined as a function of the annealing temperature T (see Supporting Information, Figure S3), demonstrating the induced increase of unit cell parameters with temperature owing to the thermal expansion.

3.3. Isothermal Heating in Air. The ground powders of ordered $ZrC_{0.6}$ (~0.2 mm in average size) were isothermally heated in air at a series of temperatures for 600 min. After the isothermal heating, the XRD patterns obtained at RT (Figure 4b) are similar to those in situ XRD results (Figure 4a). Only weak oxidation to t-ZrO_2 is observable after the heating at 350 °C. After the heating at 220 and 250 °C, the phases of both ordered $ZrC_{0.6}$ and $ZrC_{0.6}O_y$ are observable in the XRD patterns, including the superstructural peaks of both ordered carbon vacancies and ordered oxygen atoms. Owing to the oxygen diffusion from outside to inside, the existence of ordered $ZrC_{0.6}$ indicates that the oxygen atoms do not diffuse so deeply into the whole $ZrC_{0.6}$ powders. The remnant ordered $ZrC_{0.6}$ exists most probably as a small core inside the powders. After the heating at 275 and 350 °C, the peaks of ordered $ZrC_{0.6}$ disappear completely in the XRD patterns. As shown in the inset of Figure 4b, the mass increases monotonically with the heating time, and it goes to a saturation value for long enough time. For the isothermal heating at the temperatures of 260 °C, 270 °C, and 275 °C, the long enough heat treatments make the mass increase to almost the same saturation value. After the saturation, the mass increase was determined to be about 6.8% from the three TG measurements. The only observable phase of ordered $ZrC_{0.6}O_y$ in the XRD patterns indicates that the oxygen atoms go deeply into the whole powder and occupy all the vacancies, or at least most of them. From this observed mass increase of 6.8% and on the assumption that all carbon vacancies are occupied by O atoms, the carbon content in the sintered ZrC_x is refined to be 0.58, a little smaller than the estimated value of 0.61 from the oxidation route. The oxygen content of y should then be approximately equal to 0.42. Moreover, despite the coexistence of the ordered $ZrC_{0.6}$ and $ZrC_{0.6}O_y$ after the heating at the lower temperature of T < 275 °C, the reflection peaks of the ordered $ZrC_{0.6}O_y$ are not shifted in positions with respect to those of ordered $ZrC_{0.6}O_{0.4}$. It can be thus deduced that the value of y should be independent of the heating temperature and time.

3.4. Ordered O Atoms in $ZrC_{0.6}O_{0.4}$. Intuitively, the complete replacement of ordered vacancies by O atoms in Zr_2C would produce a new phase of Zr_2CO with the ordered O atoms. On the basis of the cubic superstructural model of Zr_2C,[9] the crystal structure of Zr_2CO with space group of $Fd\bar{3}m$ is constructed via the geometry optimization (see Figures 5a, 5c, and 5e). The oxygen atoms in the C sublattice have the same ordering arrangement as the carbon vacancies, and Zr_2CO is isostructural to Zr_2C. Relative to the Zr positions in Zr_2C, the Zr atoms in Zr_2CO are finely adjusted in positions owing to the ordered ionic Zr−O bonds. In comparison to Zr_2C, this fine adjustment of Zr positions in Zr_2CO can be reflected in the

dx.doi.org/10.1021/ic300014a | Inorg. Chem. 2012, 51, 5164−5172

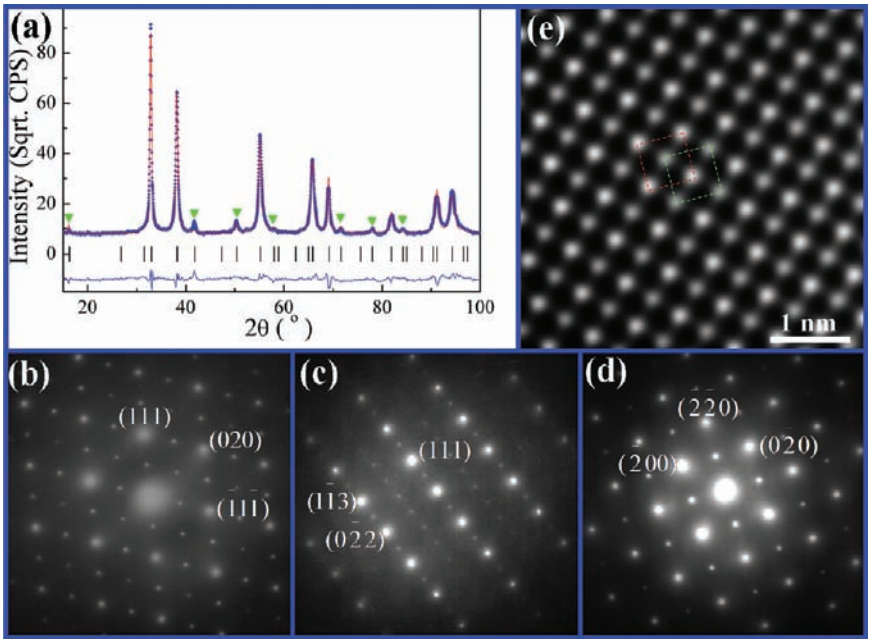

Figure 6. (a) Experimental XRD spectrum (blue diamonds) and the Rietveld refinement result (solid line) for the ordered $ZrC_{0.6}O_{0.4}$ obtained after the isothermal heating at 275 °C. The solid curve on the bottom shows the difference between the experimental and the calculated results. The vertical bars in the middle represent the positions of all possible reflections peaks. (b, c, d) The SAED patterns collected from a broken piece of the ordered $ZrC_{0.6}O_{0.4}$ along the zone axes of $[\bar{1}01]$, $[\bar{2}11]$, and [001], respectively. (e) The HRTEM image taken along the [001] zone axis.

SAED patterns along different zone axes. The SAED patterns are simulated for Zr_2CO along three different zone axes of $[\bar{1}01]$, $[\bar{2}11]$, and [001] (see Figure 5b, 5d, and 5f). Because of the fine adjustment of Zr positions and the presence of the oxygen atoms, the superstructural reflections in Zr_2CO are always observable in the SAED patterns, in contrast to the invisibility of superstructural reflections in the SAED patterns of Zr_2C along some special zone axes, for example, [001].

The ordered $ZrC_{0.6}O_{0.4}$ can be formed through the diffusion of O atoms into the ordered vacancies of ordered $ZrC_{0.6}$ after the heat treatment at 275 °C. Figure 6a shows the experimental XRD pattern together with the Rietveld refinement results for the ordered $ZrC_{0.6}O_{0.4}$. The Rietveld refinement is performed on the basis of the geometry-optimized structure model of Zr_2CO. Clearly, a good agreement is obtained between the experimental and the calculated XRD patterns. The unit cell parameter of ordered Zr_2CO is determined to be 0.93986 nm. The C, O, and Zr atoms are located at positions of 16d (5/8 5/8 5/8), 16c (1/8 1/8 1/8), and 32e (3/8 3/8 3/8), respectively. Two types of $(111)_{C(O)}$ planes and the crystal model are constructed with the Zr-octahedrons (see Supporting Information, Figure S4). Relative to the ordered $ZrC_{0.6}$, the ionic Zr−O bonds in the ordered $ZrC_{0.6}O_{0.4}$ induce the fine adjustment of the Zr positions (refer to Table 2 for the relative shift of Zr positions). The ordered $ZrC_{0.6}O_{0.4}$ is investigated via the measurements of TEM and SAED. Figures 6b, 6c, and 6d show the SAED patterns, which are obtained along three different zone axes from a broken piece of $ZrC_{0.6}O_{0.4}$. In comparison to the ordered $ZrC_{0.6}$, some new features are observed to appear in the SAEDs for $ZrC_{0.6}O_{0.4}$. These new features reflect the effects of the fine adjustment of the Zr positions and the presence of O atoms on the electron diffractions along different zone axes. To understand the effect of the shifted Zr atoms, the SAEDs have been calculated for Zr_2C, but the Zr atoms are considered to be shifted similar to those in Zr_2CO (see Supporting Information, Figure S5). In comparison with the theoretical model of Zr_2C,[9] it is demonstrated that the larger displacement of Zr atoms induces discernible changes in some of the superstructural reflections. Along the $[\bar{1}01]$ zone axis, for example, the superstructural 1/2 {313} reflections are very strong in intensity in the SAED for the theoretical model of Zr_2C, but when the shift of Zr atoms is larger, these superstructural 1/2 {313} reflections become very weak in intensity and are almost invisible. Because of the presence of atoms in Zr_2CO, however, they become stronger again in intensity in the experimental SAED. Along the [001] zone axis, for example, the superstructural 1/2{110} reflections do not appear in the SAED for the theoretical model of Zr_2C. When the larger shift of Zr atoms are considered, they become visible, but their intensity is very weak. With the presence of O atoms, however, these superstructural reflections become much stronger in intensity. Thus, the fine adjustment of Zr atom positions has impact on the SAEDs, and the impact depends on the zone axis. In comparison to the presence of O atoms, however, the impact of shifted Zr atoms is very weak. The dominant effect comes from the presence of O atoms. In the HRTEM image, the superstructural feature is also distinguishable owing to

Table 2. Refined Parameters for Carbon Vacancies Ordered $ZrC_{0.6}O_{0.4}$ Obtained from Rietveld Refinement of Powder XRD Pattern

atom	*x*	*y*	*z*	occupation	B_{iso} (Å^2)
C	0.1250	0.1250	0.1250	1	2.85
Zr	0.3702	0.3702	0.3702	1	2.02
O	0.6250	0.6250	0.6250	1	3.14

*The X-ray wavelength is 0.154056 nm. The unit cell parameter of superstructural phase of Zr_2CO is determined to be 0.93986(6) nm. The space group is $Fd\bar{3}m$. *R* factors, Sig. =1.64, R_w = 10.3%, R_{exp}= 7.327%. The displacement of Zr atoms from the ideal position of 32(e) (0.3750) is 0.0048.

dx.doi.org/10.1021/ic300014a | Inorg. Chem. 2012, 51, 5164−5172

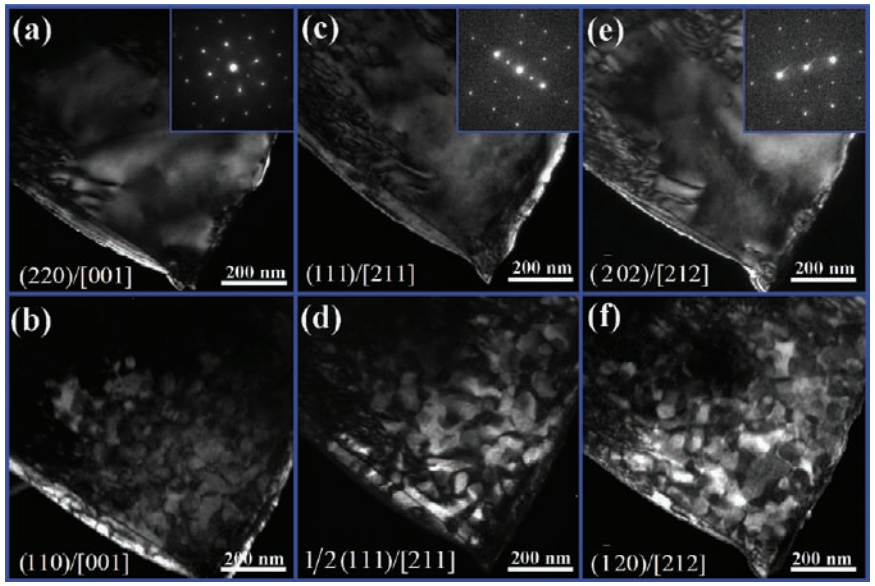

Figure 7. DF TEM images of a broken piece of the ordered $ZrC_{0.6}O_{0.4}$ and the SAED patterns along three different zone axes of [001], [211], and [212].

the changes in contrast induced by the ordering alignment of O atoms in the C sublattice, for instance, in the HRTEM image along the [001] zone axis (Figure 6e). The consistency of the XRD, SAED, and HRTEM results corroborates that the superstructure of ordered O atoms in $ZrC_{0.6}O_{0.4}$ is isostructural to the constructed one of Zr_2CO.

3.5. Nano Superstructural Domains and Lamellar Twins in $ZrC_{0.6}O_{0.4}$. Since the ordered $ZrC_{0.6}O_{0.4}$ is produced by the diffusion of O atoms into the ordered vacancies of $ZrC_{0.6}$, the occupancy of O atoms should be also ordered in nanoscale, similar to the ordered vacancies in $ZrC_{0.6}$. To investigate the ordered O atoms, the SAED patterns and the DF TEM images were taken from a broken piece of the ordered $ZrC_{0.6}O_{0.4}$ along three zone axes of [001], [211], and [212], respectively. In the collected SAED patterns as shown in insets of Figure 7, as well as the reflections from the parent rocksalt structure, the superstructural reflections induced by the ordered O atoms are observable. The sharpness of the reflections indicates the good crystallinity of the parent rocksalt structure and the superstructure. Using the reflections from the parent rocksalt structure, the obtained DF images in Figures 7a, 7c, and 7e demonstrate the relatively uniform contrast, being suggestive of the uniform contributions to the reflections from the parent rocksalt structure. Using the superstructural reflections, however, the obtained DF images in Figures 7b, 7d, and 7f reveal that the contributions to those reflections come from the separate nano domains. In other words, the ordering arrangement of O atoms in the C sublattice is restricted to separate nano domains, forming the nano superstructural domains. Moreover, different irregular shapes are observed for the bright nano domains along different zone axes. Even along the same zone axis, the observed bright domains present the different irregular shapes in the DF images taken by using the different superstructural reflections (see Supporting Information, Figure S6). From these DF images, it is recognized that the nano superstructural domains of ordered O atoms are pretty irregular in shape.

The HRTEM measurements were used to understand the atomic arrangement on the boundary surfaces between adjacent superstructural domains. The HRTEM images as shown in Figures 8a and 8b are obtained from the same broken piece of the ordered $ZrC_{0.6}O_{0.4}$, but along the different zone axes of

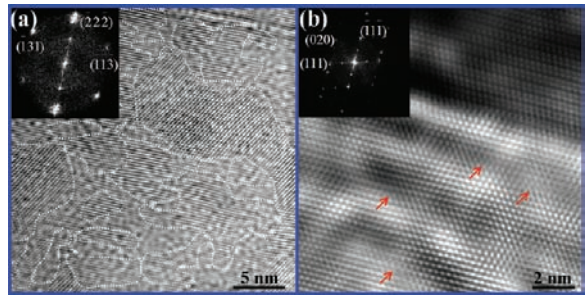

Figure 8. (**a**) Fourier-filtered HRTEM image and the corresponding FFT patterns (inset) from a broken piece of the ordered $ZrC_{0.6}O_{0.4}$ along the $[2\bar{1}1]$ zone axis. On the left top corner, a twin boundary can be distinguished. This image demonstrates the polycrystalline feature, but the FFT pattern displays the character of single crystal. The FFT pattern shows the appearance of the reflections from the parent rocksalt structure as well as the superstructural reflections from ordered O atoms. (**b**) The Fourier-filtered HRTEM image and the corresponding FFT patterns (inset) from the same broken piece along the $[\bar{1}01]$ zone axis. The image shows some lattice distortions (pointed to by arrows) and the twin boundary. In the FFT pattern, the characteristics of a twin are clearly demonstrated.

$[2\bar{1}1]$ and $[\bar{1}01]$, respectively. Along the $[2\bar{1}1]$ zone axis, the HRTEM image in Figure 8a shows the polycrystalline feature. However, the FFT pattern (inset of Figure 8a) reveals the character of a single crystal. This spurious polycrystalline feature can be attributed to the limited ordering length of the O atoms and the irregular shapes of nano domains. On the boundaries between adjacent irregular nano domains, some changes should occur in the ordering alignment of O atoms. However, owing to the significantly irregular shapes, the domain surfaces can be so greatly curved inward or outward that it is very difficult to align the electron beam parallel to the boundary surfaces. Thereby, overlapping of different atomic planes can occur in the HRTEM measurements. As shown in the enlarged HRTEM image of Figure 8b along the $[\bar{1}01]$ zone axis, some spurious lattice

dx.doi.org/10.1021/ic300014a | *Inorg. Chem.* 2012, 51, 5164−5172

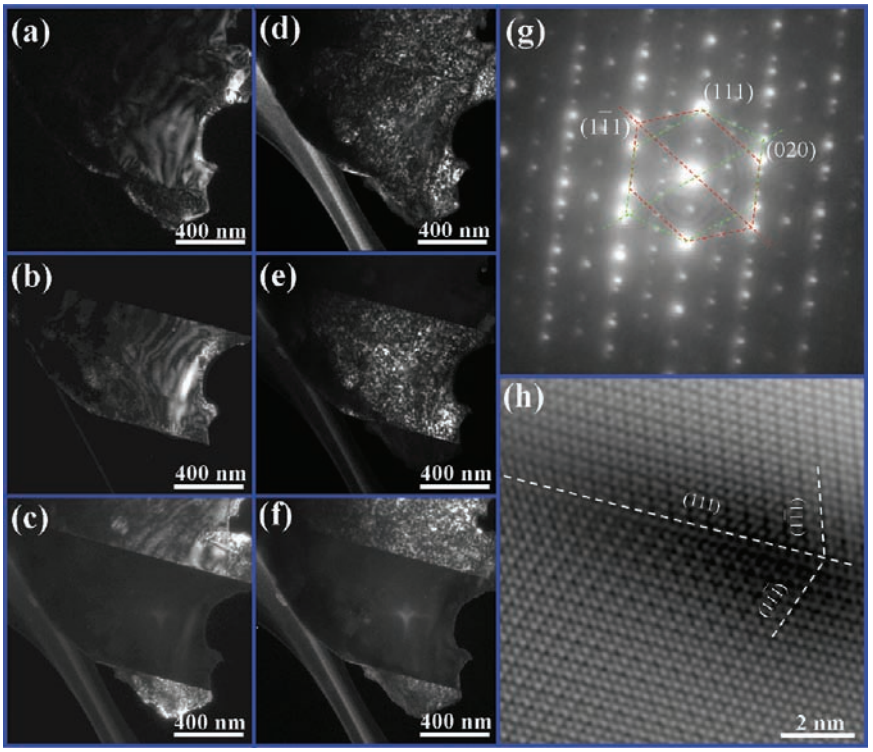

Figure 9. (**a, b, c**) DF TEM images of a broken piece of the ordered $ZrC_{0.6}O_{0.4}$, which are obtained via the reflections of (111), (1$\bar{1}$1), and $(1\bar{1}1)_t$, respectively, from the parent rocksalt structure along the [$\bar{1}$01] zone axis. (**d, e, f**) The DF TEM images of this broken piece, which are taken via the superstructural reflections of 1/2(111), 1/2(1$\bar{1}$1), and $1/2(1\bar{1}1)_t$, respectively, along the [$\bar{1}$01] zone axis. (**g**) The SAED pattern collected from this broken piece along the [$\bar{1}$01] zone axis, in which the twin relations are marked out. (**h**) The HRTEM image along the [$\bar{1}$01] zone axis, in which the twin plane is pointed out.

distortions are observed on the domain boundaries. Actually, these spurious lattice distortions are created by the overlapping of different atomic planes.

Interestingly, twins are observed in a small amount of particles with the help of TEM. As shown in Figure 9, via the measurements of SAED, DF TEM images, and HRTEM images, it is found that this broken piece of ordered $ZrC_{0.6}O_{0.4}$ is composed of the lamellar twins. The DF TEM images in Figures 9a–9g are taken along the [$\bar{1}$01] zone axis. Figures 9a, 9b, and 9c are the DF images obtained by using the reflections of (111), (1$\bar{1}$1), and $(1\bar{1}1)_t$, respectively, from the parent rocksalt structure. Figures 9d, 9e, and 9f are the DF images obtained via the superstructural reflections of 1/2(111), 1/2(1$\bar{1}$1), and $1/2(1\bar{1}1)_t$, respectively. In these DF images, the lamellar twins are clearly recognized not only in the parent rocksalt structure but also in the superstructure, although the ordered O atoms are constrained to the separated nano domains. The twin relations are clearly demonstrated in the SAED pattern of Figure 9g and the HRTEM image of Figure 9h. The twin plane and angle are determined to be {111} and 70.53°, respectively. Only {111}-specific twins are observed in our sample.

4. CONCLUSIONS

In summary, via the heat treatments of the ordered $ZrC_{0.6}$ at low temperature, it is revealed that the vacancy channels in the C sublattice provide the additional fast tracks for the oxygen diffusion, favoring the diffusion of O atoms into the vacancies. The O atoms are thermally activated to go directly into and occupy the vacancies, thus forming the ordered phase of oxycarbide $ZrC_{0.6}O_{0.4}$. Similar to the carbon vacancies in the ordered $ZrC_{0.6}$, the O atoms in the ordered $ZrC_{0.6}O_{0.4}$ have the ordering alignment at the nanoscale, thus forming the nano superstructural domains. In comparison to the ordered $ZrC_{0.6}$, the existence of ionic Zr−O bonds in the ordered $ZrC_{0.6}O_{0.4}$ induces the fine adjustment of the Zr positions. Thereby, in contrast to the invisibility of the superstructural reflections from ordered carbon vacancies along some special zone axes, the superstructural reflections owing to ordered O atoms are always observable in the SAED patterns. Via the TEM, SAED, and HRTEM measurements along different zone axes, it is recognized that the superstructural domains have significantly irregular shapes. The outside surfaces of the domains can be highly curved inward or outward. Thus, it is very difficult to tune the electron beam parallel to the interfaces, making it hard to unveil the atomic arrangement on the boundary interfaces between the superstructural domains via the HRTEM images. Interestingly, the lamellar twins are observed in the ordered $ZrC_{0.6}O_{0.4}$. The twin plane and twin angle are determined to be {111} and 70.53°, respectively.

■ ASSOCIATED CONTENT

Ⓢ Supporting Information

The constructed structures with C atom centered Zr-octahedrons on the basis of the superstructural model of Zr_2C, two types of $(111)_C$ planes, and the crystal model viewed along the [$\bar{1}$01] zone axis (Figure S1). The XEDS results obtained from a polished sheet of the ordered $ZrC_{0.6}$ before and after the heat treatment (Figure S2a). Inset of Figure S2a showing the color change from silver gray to golden yellow induced by the heating. The color change to golden yellow after the exposure under atmospheric environment for about 6 months (Figure S2b). The change of unit cell parameters with

dx.doi.org/10.1021/ic300014a | Inorg. Chem. 2012, 51, 5164−5172

the increase of annealing temperature for both $ZrC_{0.6}$ and $ZrC_{0.6}O_{0.4}$ (Figure S3). The constructed structures with C (O) atom centered Zr-octahedrons on the basis of the superstructural model of Zr_2CO, two types of $(111)_{C(O)}$ planes and the crystal model viewed along the $[\bar{1}01]$ zone axis (Figure S4). The calculated SAED patterns along two different zone axes for the theoretical models of Zr_2C[9] and Zr_2C with the shift of Zr atoms similar to Zr_2CO, the experimental SAED patterns of Zr_2CO (Figure S5). The DF images and SAED patterns collected along the [212] axis from a broken piece of the ordered $ZrC_{0.6}O_{0.4}$ (Figure S6). This material is available free of charge via the Internet at http://pubs.acs.org.

AUTHOR INFORMATION

Corresponding Author

*E-mail: liuzy0319@yahoo.com (Z.L.), fhcl@ysu.edu.cn (Y.T.). Fax: +86 335 8074545.

Notes

The authors declare no competing financial interest.

ACKNOWLEDGMENTS

We are thankful for the financial support from the National Science Fund for Distinguished Young Scholars (Grant 51025103) and the National Basic Research Program of China (Grants 2010CB731605, 50872118, and 58021001).

REFERENCES

(1) Pierson, H. O. *Handbook of Refractory Carbides and Nitrides -Properties, Characteristics, Processing and Applications*; William Andrew Publishing/Noyes: Westwood, NJ, 1996.
(2) Oyama, S. T. *The Chemistry of Transition Metal Carbides and Nitrides*; Blackie Academic & Professional: Glasgow, U.K., 1996.
(3) Toth, L. E. *Transition Metal Carbides and Nitrides*; Academic Press: New York, 1971.
(4) Ogawa, T.; Ikawa, K. *J. Nucl. Mater.* **1982**, *105*, 331.
(5) Chang, J. h.; Kim, Y.; Lee, K.; Lee, Y.; Lee, W. J.; Noh, J.; Kim, M.; Lim, H.; Shin, Y.; Bae, K.; Jung, K. *Nucl. Eng. Technol.* **2007**, *39*, 111.
(6) Shimada, S.; Inagaki, M.; Suzuki, M. *J. Mater. Res.* **1996**, *11*, 2594.
(7) Shimada, S. *J. Ceram. Soc. Jap.* **2001**, *109*, S33.
(8) Shimada, S. *Solid State Ionics* **2002**, *149*, 319.
(9) Gusev, A. I.; Rempel, A. A. *Phys. Status Solidi A* **1993**, *135*, 15.
(10) Lipatnikov, V. N.; Rempel, A. A.; Gusev, A. I. *Int. J. Refract. Met. Hard Mater.* **1997**, *15*, 61.
(11) Zueva, L. V.; Lipatnikov, V. N.; Gusev, A. I. *Inorg. Mater.* **2000**, *36*, 695.
(12) Lipatnikov, V. N.; Lengauer, W.; Ettmayer, P.; Keil, E.; Groboth, G.; Kny, E. *J. Alloys Compd.* **1997**, *261*, 192.
(13) Morgan, G.; Lewis, M. H. *J. Mater. Sci.* **1974**, *9*, 349.
(14) Valeeva, A.; Davydov, D.; Rempel, S.; Rempel, A. *Inorg. Mater.* **2009**, *45*, 905.
(15) Miracle, D. B.; Lipsitt, H. A. *J. Am. Ceram. Soc.* **1983**, *66*, 592.
(16) Tsurekawa, S.; Kurishita, H.; Yoshinaga, H. *J. Nucl. Mater.* **1989**, *169*, 291.
(17) Gringoz, A.; Glandut, N.; Valette, S. *Electrochem. Commun.* **2009**, *11*, 2044.
(18) De Novion, C. H.; Moisy-Maurice, V. *J. Phys. Colloques.* **1977**, *38*, C7.
(19) De Novion, A. H.; Landesman, J. P. *Pure Appl. Chem.* **1985**, *57*, 1391.
(20) Lipatnikov, V. N.; Kottar, A.; Zuvea, L. V.; Gusev, A. I. *Inorg. Mater.* **2000**, *35*, 155.
(21) Xiang, J. Y.; Hu, W. T.; Liu, S. C.; Chen, C. K.; Zhang, Y.; Wang, P.; Wang, H. T.; Wen, F. S.; Xu, B.; Yu, D. L.; He, J. L.; Tian, Y. J.; Liu, Z. Y. *Mater. Chem. Phys.* **2011**, *130*, 352.
(22) Xiang, J. Y.; Liu., S. C.; Hu, W. T.; Zhang, Y.; Chen, C. K.; Wang, P.; He, J. L.; Yu, D. L.; Xu, B.; Lu, Y. F.; Tian, Y. J.; Liu, Z. Y. *J. Eur. Ceram. Soc.* **2011**, *31*, 1491.
(23) Kosolapova, T. Y.; Fedorus, V. B.; Panasyuk, A. D.; Kozina, G. K. *Powder Metall Met. Ceram.* **1972**, *109*, 47.
(24) Gozzi, D.; Montozzi, M.; Cignini, P. L. *Solid State Ionics* **1999**, *123*, 1.
(25) Gendre, M.; Maitre, A.; Trolliard, G. *J. Eur. Ceram. Soc.* **2011**, *31*, 2377.
(26) Barnier, P.; Thévenot, F. *Int. J. High Technol. Ceram.* **1986**, *2*, 291.
(27) Ouensanga, A. H.; Dodé, M. *Rev. Int. Htes. Temp. Réfract.* **1974**, *11*, 35.
(28) Leprince-Ringuet, F.; Lejus, A. M.; Collongues, R. *C. R. Acad. Sci. Fr.* **1964**, *258*, 221.
(29) Stirns, E. K. *The refractory carbides*; Academic Press: New York, 1967.
(30) Cruz Fernandes, J.; Amaral, P. M.; Guerra Rosa, L. *Int. J. Refract. Met. Hard Mater.* **1999**, *17*, 437.